BIOMICROFLUIDICS **12**, 014108 (2018)

Helical micropumps near surfaces

Justas Dauparas, Debasish Das, and Eric Lauga[a)]
Department of Applied Mathematics and Theoretical Physics, University of Cambridge, Cambridge, CB3 0WA, United Kingdom

(Received 5 November 2017; accepted 4 January 2018; published online 19 January 2018)

Recent experiments proposed to use confined bacteria in order to generate flows near surfaces. We develop a mathematical and a computational model of this fluid transport using a linear superposition of fundamental flow singularities. The rotation of a helical bacterial flagellum induces both a force and a torque on the surrounding fluid, both of which lead to a net flow along the surface. The combined flow is in general directed at an angle to the axis of the flagellar filament. The optimal pumping is thus achieved when bacteria are tilted with respect to the direction in which one wants to move the fluid, in good agreement with experimental results. We further investigate the optimal helical shapes to be used as micropumps near surfaces and show that bacterial flagella are nearly optimal, a result which could be relevant to the expansion of bacterial swarms. *Published by AIP Publishing.* https://doi.org/10.1063/1.5012070

I. INTRODUCTION

Transporting fluid on small scales is an important but complex problem. Various pumping mechanisms are observed in nature, from fluid being pushed by muscles in the walls of the lymphatic vessels,[1] sodium-potassium pumps in the membranes of cells,[2] and efficient osmotic pumping in plants[3] to cilia-induced flows in major organs including the brain,[4] the respiratory system,[5] and reproductive tracts.[6]

Some of these transport mechanisms inspired the design of pumps for microfluidic systems which may be used for biological and chemical sensing, drug delivery, molecular separation, amplification, and sequencing.[7] There are two major classes of such pumps: mechanical displacement pumps, which apply forces to fluids via moving boundaries, and electro- and magnetokinetic pumps which provide energy to fluids continuously and as a result generate flow.[8] Mechanical or electrokinetic micropumps are used in the majority of lab-on-a-chip devices that require powered fluid flow, but the technical challenges and the requirement of external power associated with these pumping devices have impeded their miniaturisation.

Self-powered micropumps have been designed to address some of these issues.[9] One of the solutions is to build bio-hybrid cell-based actuators. Recently, there has been growing interest in using live biological cells to produce devices that work as microscopic gears,[10] microrotors,[11] micropumps,[12] microswimmers,[13] and microwalkers.[14] Bacterial carpets, which are surface arrays of fixed bacteria,[15,16] can also create linear and rotational flows[17] and enhance mixing.[18]

In this work, we focus on bacterial micropumps, with their potential to be used for automation of chemistry and biology.[19] In one of the first bacterial micropump experiments, *Escherichia coli* cells were tethered to microchannel walls by a single flagellar filament and the bodies of the cells would rotate at about 10 rps, thereby pumping fluid from one end of the channel to the other.[20,21] In another experiment, cells were attached to the surface by their bodies with flagella free to rotate,[12] demonstrating that the bacteria are able to self-organise, generating a collective flow that can pump fluid autonomously through a microfabricated channel. Furthermore, the addition of glucose to the working buffer raises the metabolic activity of the bacterial carpet, resulting in enhanced pumping performance.

[a)] Electronic mail: e.lauga@damtp.cam.ac.uk

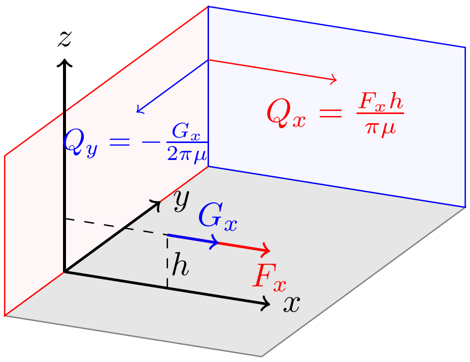

FIG. 1. A point force $\mathbf{F} = (F_x, 0, 0)$ and a point torque $\mathbf{G} = (G_x, 0, 0)$ located at $(0, 0, h)$ above the infinite plane at $z = 0$ generate a net hydrodynamic flux $\mathbf{Q} = F_x h/(\pi\mu)\mathbf{e}_x - G_x/(2\pi\mu)\mathbf{e}_y$.

In this paper, we consider the bacterial pumping system described in a recent experimental paper where *E. coli* bacteria were confined within micro-fabricated structures in a prescribed geometrical configuration and whose flagellar rotation collectively generated flow that can transport materials along designed trajectories.[22] This study naturally raises the question of (i) how the performance of the resulting pumps depends on the detailed geometrical characteristics of the microscopic cages in which the cells are trapped and (ii) how to optimise them. In order to answer these questions, we use the mathematical techniques of resistive-force theory (RFT)[23] and slender-body theory (SBT)[24,25] to model the flow induced by the rotating flagellar filaments of the trapped bacteria. We first quantify how the magnitude and direction of the bacteria-driven pump depend on the configuration of the flagella and then address the geometrical optimisation of the helical shapes used to generate the flow.

II. FLUX INDUCED BY HELIX ROTATING ABOVE A WALL

In this section, we derive a mathematical model to compute the flux produced by a fixed bacterium whose flagellar filaments are rotating above a no-slip wall. Both resistive-force theory (analytical approach) and slender-body theory (computational approach) are used and we compare our results with experimental measurements of Ref. 22.

A. Flux due to singularities above a wall

Consider a Cartesian coordinate system (x, y, z) with unit vectors $(\mathbf{e}_x, \mathbf{e}_y, \mathbf{e}_z)$, as illustrated in Fig. 1. A point force (Stokeslet) $\mathbf{F} = F_x\mathbf{e}_x$ is located at a height h above an infinite no-slip wall with normal $\mathbf{e}_z$ in a fluid with dynamic viscosity μ. Assuming the flow to have no inertia, which is a reasonable assumption on the small length scales of bacteria,[22] the resulting solution to the incompressible Stokes equations has a velocity field denoted by $\mathbf{u}$. It is a classical (and exact) result that this point force will then produce a net flux (i.e., flow rate)[26,27] given by

$$\begin{aligned}\mathbf{Q}_F &= \int_0^{\infty}\int_{-\infty}^{\infty}(\mathbf{u}\cdot\mathbf{e}_x)\mathbf{e}_x dydz + \int_0^{\infty}\int_{-\infty}^{\infty}(\mathbf{u}\cdot\mathbf{e}_y)\mathbf{e}_y dxdz \\ &\quad + \int_{-\infty}^{\infty}\int_{-\infty}^{\infty}(\mathbf{u}\cdot\mathbf{e}_z)\mathbf{e}_z dxdy \\ &= \frac{F_x h}{\pi\mu}\mathbf{e}_x,\end{aligned} \tag{1}$$

which is in the same direction as the force (see Fig. 1). The calculation for the flux is summarised in Appendix A. Physically, while the flow induced by a point force decays as $1/r$, a point force near a wall decays faster as $1/r^2$ and since the area of integration scales as distance squared, a net flow rate is obtained in Eq. (1).

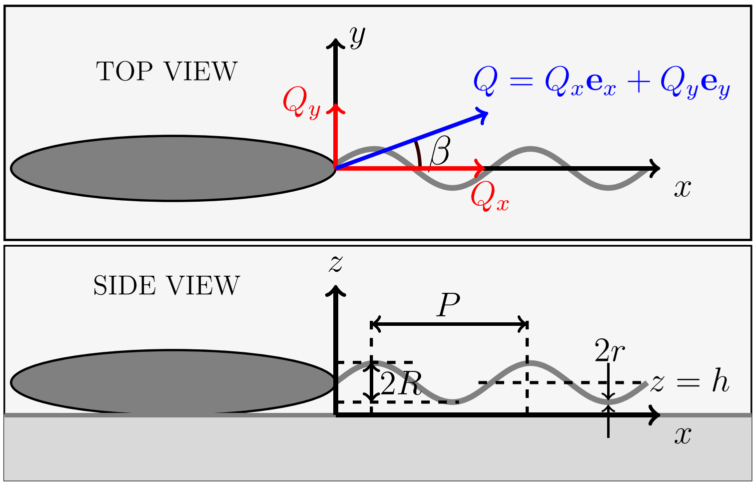

FIG. 2. Top and side view of a bacterium with a helical bundle of flagellar filaments. The helical bundle has pitch P, and radius R, while the bundle radius is denoted by r. The axis of the helix is positioned at height h above the surface. With the cell body stuck, the rotating bundle creates a net flow parallel to the surface with flow rate $\mathbf{Q} = Q_x\mathbf{e}_x + Q_y\mathbf{e}_y$, and thus at an angle $\tan\beta = Q_y/Q_x$ to the x direction.

Similarly, a point torque (Rotlet) $\mathbf{G} = G_x\mathbf{e}_x$ placed at the same location will produce exactly the net flux

$$\mathbf{Q}_G = -\frac{G_x}{2\pi\mu}\mathbf{e}_y, \tag{2}$$

which points in the direction perpendicular to both the torque and the surface (see the derivation in Appendix B).

B. Flagellar flows as one singularity

Most motile bacteria, including *E. coli*, are propelled by the rotation of helical flagellar filaments.[28] Each filament is attached to the cell body via a short flexible hook itself connected to a bacterial rotary motor. The so-called "normal" shape of the flagellar filament is a left-handed helix, typically rotated in the counter-clockwise (CCW) direction when viewed from behind the cell. An *E. coli* bacterium has approximately 4 flagella on the body[29] which normally bundle in the back of the cell forming a thick effective helix.[28]

The simplest model for the flow induced by a rotating bundle of flagellar filaments near a surface consists of computing the net force, **F**, and torque, **G** which the bundle applies on the fluid and use the result from Sec. II A. In this simple model, we neglect the presence of the cell body on the fluid flow because only a small portion of the flagellar bundle is near the cell body, while the majority of the bundle is closer to the no-slip wall. Let us then assume that we have a perfect helix parallel to a no-slip wall whose axis is at height $z = h$ with the wall at $z = 0$ (see Fig. 2).

In order to relate the values of **F** and **G** to the geometry of the helical bundle, we use resistive-force theory (RFT) which captures the density of hydrodynamic forces acting on slender filaments in Stokes flows.[23] We denote by $\xi_\perp$ the drag coefficient (i.e., force per unit length) for translation of a portion of the filament bundle locally perpendicular to its tangent and $\xi_\parallel$ the drag coefficient in the parallel direction and we write their ratio as $\rho = \xi_\parallel/\xi_\perp$. We will use the drag coefficients obtained by Lighthill[23] as

$$\xi_\parallel = \frac{2\pi\mu}{\ln(0.18P\sec\Psi/r)}, \quad \xi_\perp = \frac{4\pi\mu}{1/2 + \ln(0.18P\sec\Psi/r)}, \tag{3}$$

where we denote μ the dynamic viscosity of fluid, r the bundle radius, R the helix radius (i.e., the radius of the cylinder on which its centreline is coiled), P its pitch, and Ψ the pitch angle (i.e., $\tan \Psi = 2\pi R/P$), as shown in Fig. 2. The axis of the helix axis is assumed to be directed along the x direction and we use cylindrical coordinates (σ, θ, x) around the helix axis.

It is a classical result[30] that the force per unit length acting on the fluid by a counter-clockwise (CCW, i.e., in the positive x direction) rotating left-handed helix has components

$$f_\theta = \xi_\perp R\omega(\cos^2\Psi + \rho\sin^2\Psi), \tag{4}$$

$$f_x = \xi_\perp R\omega(1-\rho)\sin\Psi\cos\Psi, \tag{5}$$

$$f_\sigma = 0, \tag{6}$$

where ω denotes the angular velocity of the helix. The total force acting on the fluid and the total torque about the axis of the helix are obtained by integrating the force density along the arc length $0 \le s \le L$ leading to

$$F_x = \int_0^L f_x ds = \xi_\perp R\omega(1-\rho)\sin\Psi\cos\Psi L, \tag{7}$$

$$G_x = \int_0^L f_\theta R ds = \xi_\perp R^2\omega(\cos^2\Psi + \rho\sin^2\Psi)L, \tag{8}$$

where L is the total contour length of the helix. Using the result of Sec. II A, these force and torque induce a net flow rate of

$$\mathbf{Q} = \frac{F_x h}{\pi\mu}\mathbf{e}_x - \frac{G_x}{2\pi\mu}\mathbf{e}_y. \tag{9}$$

Using Q to denote the magnitude of the flux and β the angle between the net flow and the x axis (see Fig. 2), Eq. (9) leads to

$$Q^2 = \left(\frac{F_x h}{\pi\mu}\right)^2 + \left(\frac{G_x}{2\pi\mu}\right)^2, \quad \beta = -\arctan\left(\frac{G_x}{2F_x h}\right). \tag{10}$$

If we substitute the expression for the force and the torque from Eqs. (7) to (8), the model leads to the prediction

$$Q^2 = \left(\frac{\xi_\perp R\omega(1-\rho)\sin\Psi\cos\Psi L h}{\pi\mu}\right)^2 + \left(\frac{\xi_\perp R^2\omega(\cos^2\Psi + \rho\sin^2\Psi)L}{2\pi\mu}\right)^2, \tag{11}$$

$$\beta = -\arctan\left(\frac{(\cos^2\Psi + \rho\sin^2\Psi)R}{2(1-\rho)\sin\Psi\cos\Psi h}\right). \tag{12}$$

C. Flagellar flows as a superposition of singularities

The approach in Sec. II B modelled the helix as a single force and torque singularity. Alternatively, we may write the helix as a superposition of flow singularities. The centreline of the left-handed helix may be parametrised as $[x_0(s, t), y_0(s, t), z_0(s, t)]$ with

$$x_0(s,t) = s\cos\Psi, \tag{13}$$

$$y_0(s,t) = -R\sin\left(\omega t - 2\pi\frac{s}{P}\cos\Psi\right), \tag{14}$$

$$z_0(s,t) = h - R\cos\left(\omega t - 2\pi\frac{s}{P}\cos\Psi\right), \tag{15}$$

where s denotes the arclength along the helix centreline and t time. As a result, the total flow rate has

$$Q_x(t) = \frac{1}{\pi\mu}\int_0^L f_x(s) z_0(s,t) ds, \tag{16}$$

$$Q_y(t) = \frac{1}{\pi\mu}\int_0^L f_y(s,t) z_0(s,t) ds = \frac{1}{\pi\mu}\int_0^L f_\theta(s) \cos\left(\omega t - 2\pi \frac{s}{P}\cos\Psi\right) z_0(s) ds. \tag{17}$$

If we average over time, then we get the same results as before considering the point force and the point torque, namely, Eqs. (11)–(12).

D. Numerical approach: Slender-body theory

In parallel to the analytical approach, we may use the improved, computational model termed slender-body theory (SBT).[24] Under this framework, there is a linear relationship between the rigid body motion defined by the centreline velocity **u** and the hydrodynamic force density **f** on the fluid formally written as[25]

$$8\pi\mu \mathbf{u}(\mathbf{x},t) = -\boldsymbol{\Lambda}[\mathbf{f}](s) - \mathbf{K}[\mathbf{f}](s), \tag{18}$$

where the local, $\boldsymbol{\Lambda}$, and the non-local operators, $\mathbf{K}$, are, respectively, given by

$$\boldsymbol{\Lambda}[\mathbf{f}](s) = [-c(\mathbf{I} + \hat{\mathbf{s}}\hat{\mathbf{s}}) + 2(\mathbf{I} - \hat{\mathbf{s}}\hat{\mathbf{s}})]\cdot \mathbf{f}(s), \tag{19}$$

$$\mathbf{K}[\mathbf{f}](s) = \int_0^L \left(\mathbf{G}(s,s')\cdot \mathbf{f}(s') - \frac{\mathbf{I} + \hat{\mathbf{s}}\hat{\mathbf{s}}}{|s-s'|}\cdot \mathbf{f}(s)\right) \mathrm{d}s', \tag{20}$$

where $\mathbf{G}$ is the Stokeslet singularity defined as

$$G_{ij}(s,s') = \frac{\delta_{ij} + \hat{R}_i\hat{R}_j(s,s')}{R(s,s')}, \quad \mathbf{R} = \mathbf{x}(s) - \mathbf{x}(s'), \quad \hat{\mathbf{s}} = \frac{\partial \mathbf{x}(s)}{\partial s}, \quad \mathbf{I}_{ij} = \delta_{ij}, \tag{21}$$

where $i, j = \{1, 2, 3\}$, s is the parametric arc length of the object and the constant $c = \log(\epsilon^2 e)$. The parameter that defines slenderness is $\epsilon = r/L$, r and L being the cross-sectional radius and total arc length of the slender object.

We solve Eq. (18) numerically in order to obtain the force distribution on a helix that undergoes rigid-body rotation. The helix is divided into small straight segments over which the force and velocity are assumed to be constant. This gives rise to a linear system of the form $u_i = M_{ij} f_j$ that can be solved for the velocity if the force distribution is known, or inverted to find the force distribution if the velocity is known (which is the case here since the rotation is being prescribed).

In order to account for the presence of wall, we place the slender helix in a semi-infinite domain above a rigid boundary. The first term in the non-local operator $\mathbf{K}$, Eq. (20), contains the self-interactions of the slender filament. To include the presence of the rigid wall at $z = 0$, we place image singularities for a Stokeslet[26] on the opposite side of the wall for each element of the slender object so as to satisfy the no-slip boundary condition on the wall exactly. The operator $\mathbf{K}$ is then modified as

$$\mathbf{K}[\mathbf{f}](s) = \int_0^L \left(\left[\mathbf{G}(s,s') + \mathbf{G}^{im}(s,s')\right]\cdot \mathbf{f}(s') - \frac{\mathbf{I} + \hat{\mathbf{s}}\hat{\mathbf{s}}}{|s-s'|}\cdot \mathbf{f}(s)\right) \mathrm{d}s', \tag{22}$$

where $\mathbf{G}^{im}$ is the image of the Stokeslet

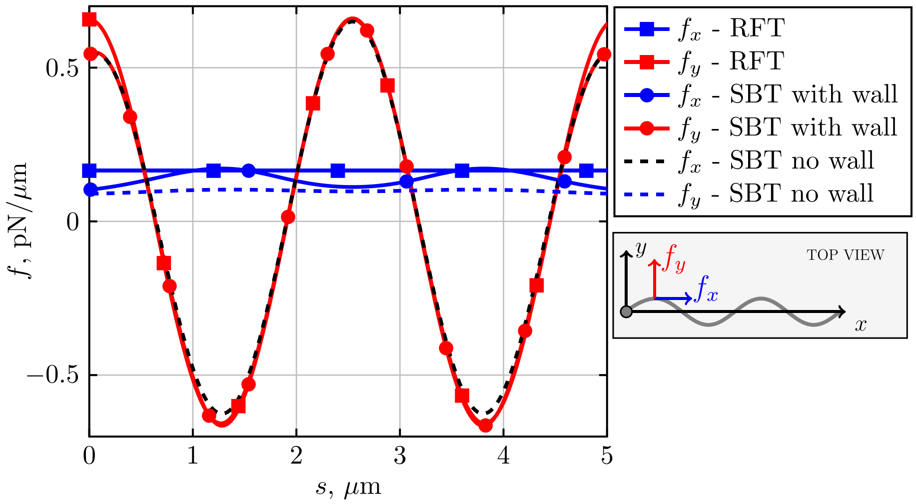

FIG. 3. Comparison between the analytical (RFT) and numerical (SBT) results for the components of the hydrodynamic force density **f** as a function of arc length, s, for *E. coli*'s helical filament rotating above the no-slip wall at height $h = 0.65\ \mu$m. Geometrical values are taken from Ref. 22.

$$G_{ij}^{im} = -\frac{\delta_{ij} + \hat{R}_i^{im}\hat{R}_j^{im}}{R^{im}} + 2h\Delta_{jk}\frac{\partial}{\partial R_k^{im}}\left(\frac{h\hat{R}_i^{im}}{R^{im2}} - \frac{\delta_{i3} + \hat{R}_i^{im}\hat{R}_3^{im}}{R^{im}}\right), \tag{23}$$

where $h = R_3$ is the distance from the wall, $\mathbf{R}^{im}(s, s') = \mathbf{x}(s) - \mathbf{x}^{im}(s')$, and $\mathbf{x}^{im} = [R_1, R_2, -R_3]$. The coefficients Δ_{jk} take the value of 1 when $j = k = 1$, 2, and −1 when $j = k = 3$ and is 0 for every other combination. We can then solve Eq. (18) numerically as above using the modified operator **K**. The obtained force distribution **f** is shown in Fig. 3. We next integrate the force density on the fluid, **f**, along the arc length of the helix to obtain the total force and torque along the helix axis and the resulting flow rate

$$\mathbf{F} = \int_0^L \mathbf{f}\,ds, \tag{24}$$

$$\mathbf{G} = \int_0^L R(\mathbf{e}_\sigma \times \mathbf{f})\,ds, \tag{25}$$

$$\mathbf{Q} = \frac{1}{\pi\mu}\int_0^L \mathbf{f}_\parallel h(s)\,ds, \tag{26}$$

where $(\mathbf{e}_\sigma, \mathbf{e}_\theta, \mathbf{e}_x)$ are the cylindrical coordinates with the flagellar axis along x and $\mathbf{f}_\parallel$ is the force density component parallel to the no-slip wall at $z = 0$, i.e., $\mathbf{f}_\parallel = \mathbf{f} - (\mathbf{f}\cdot\mathbf{e}_z)\mathbf{e}_z$.

E. Comparing analytical model with computations

We may compare the results from the analytical RFT model with the numerical SBT approach by using the set of parameters applicable to *E. coli* bacteria,[22] namely $P = 2\ \mu$m, $R = 0.25\ \mu$m, $L_{axial} = 4\ \mu$m, $r = 12$ nm, $f = 165$ Hz, and $h = 0.65\ \mu$m. Force distributions parallel (i.e., along the x direction) and perpendicular to the helical axis (i.e., along the y direction) are shown in Fig. 3. The main difference between the SBT with and without the hydrodynamic presence of the wall is that adding the wall slightly increases the force component f_x and leads to small end effects. The analytical model (RFT) which is much simpler to implement and does not include the effect of the wall is in good agreement with SBT despite a small but systematic overestimation of the force f_x. Interestingly, the forces parallel to the no-slip wall, i.e., f_x, f_y, are not very sensitive to the presence of the wall.

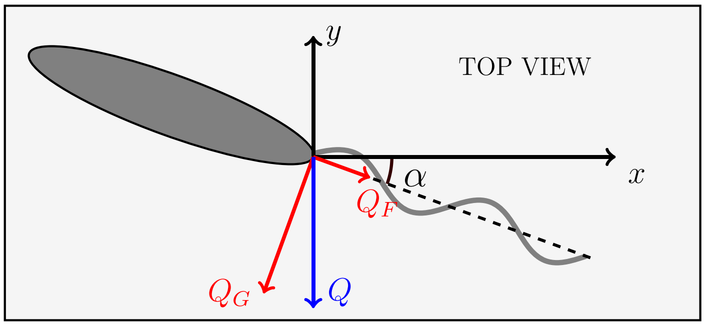

FIG. 4. Top view of a bacterium with a rotating flagellar filament. The angle between the axis of the filament and the normal to direction of the net flux Q is denoted by α. The flow rate due to the force has magnitude Q_F, while that due to the torque is denoted Q_G.

F. Comparison between theory and experiments

Using the parameters for *E. coli*,[22] we may compute the magnitude of the flow rate, Q, and its direction, β, produced by the rotating flagellar filament. Experimentally, one would like to pump the fluid along a specific direction at the maximum rate, say the negative y direction. If we define the angle α as the angle between the helix axis and the x axis such that the flux vector is along negative y direction (Fig. 4) and given the definition of β shown in Fig. 2 (top), then one should position the cell at the optimal angle α such that $\alpha = \pi/2 + \beta$.

We use our theory and computations to compute the value of this optimal angle, α, and the resulting magnitude of the flow rate, Q. We obtain results in excellent agreement with each other, namely

$$\text{RFT}: \ \alpha = 52.5^\circ,\ Q = 219\,\mu\text{m}^3/\text{s},\ F = 0.838\,\text{pN},\ G = 835\,\text{pN}\cdot\mu\text{m}, \tag{27}$$

$$\text{SBT}: \ \alpha = 50.6^\circ,\ Q = 182\,\mu\text{m}^3/\text{s},\ F = 0.712\,\text{pN},\ G = 832\,\text{pN}\cdot\mu\text{m}. \tag{28}$$

In Ref. 22, Gao *et al.* conducted experiments with *E. coli* bacteria and performed numerical simulations on the fluid flow due to trapped bacteria which were placed at angles 0°, 20°, 40°, and 60° with respect to the x axis (using our notation). It was found that among those values, the maximum flow rate was obtained for an angle of 40°. Our theoretical approach agrees with their results. Furthermore, we are able to predict that the configuration with $\alpha \approx 50^\circ$ is the best one for the use of these cells to pumps fluids.

G. Fluid flow visualisation

In order to gain further understanding of the flow due to the superposition of the two flow singularities above the no-slip wall (Stokeslet and Rotlet), we plot in Fig. 5 the streamlines and contour lines of the velocity magnitude, $u = (u_x^2 + u_y^2)^{1/2}$, on the plane at height $z = 2.1\,\mu$m above the wall (with geometrical parameters from Ref. 22). Specifically, we plot in Fig. 5(a) the flow due to the point force only, in Fig. 5(b) the flow due to the point torque only and Fig. 5(c) shows the superposition of these two flows. As expected, the combination of pushing of the fluid along the helix and rotating the helix, we clearly observe a flow occurring at an angle to the helix orientation.

A comparison between the flow field predicted by the analytical RFT model in the case when we pick $\alpha = 40^\circ$ and the experimental measurements of Ref. 22 in the same configuration is shown in Fig. 6. The flow field predicted by the theory is qualitatively similar to the experimentally obtained one and in both cases, we can clearly see the localised flow occurring mostly along the y axis. Note that the experimental flow is about half as strong as the theoretically predicted one which is due to the fluid being stopped by the presence of the boxes which trap bacteria and which are absent in our theory (they essentially provide a vertical no-slip wall at $x = 0\,\mu$m).

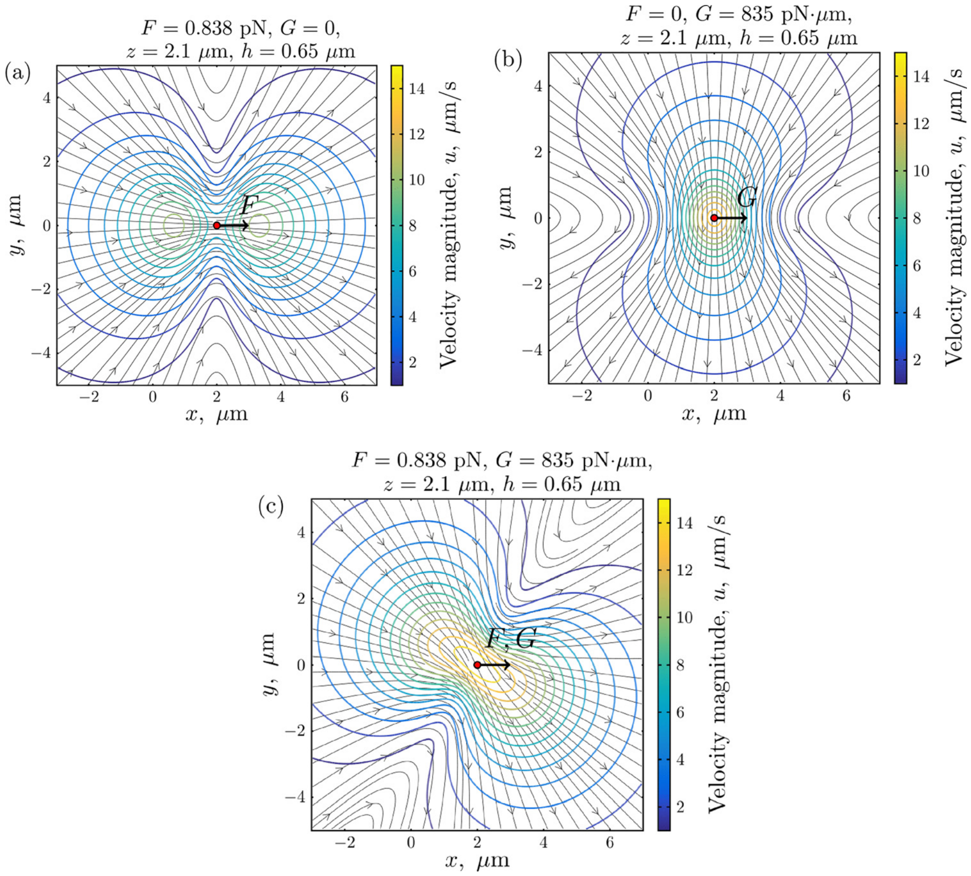

FIG. 5. Streamlines and contour lines of the two-dimensional velocity magnitude for the helix modelled as a point force F and a point torque G at the height h above the no-slip wall. (a) Fluid flow due to the point force only; (b) Flow due to torque only; (c) Combined flow due to both singularities.

H. Dependence on the distance to the wall

So far, we have assumed that the distance between the cells and the surface was a fixed height, h. If the helical filament was placed closer or further from the bottom surface, how would this impact the value of the optimal angle α? Our theoretical and computational models (RFT and SBT) allow us to investigate how the flux magnitude, Q, and the optimal angle, α, depend on the value of h, with results shown in Fig. 7.

We obtain that the analytical and numerical results are in good agreement. Furthermore, the analytical model predicts the optimal angle using Eq. (12) which is given by

$$\alpha = \arctan\left(\frac{2Fh}{G}\right) = \arctan\left(\frac{2(1-\rho)\sin\Psi\cos\Psi h}{(\cos^2\Psi + \rho\sin^2\Psi)R}\right), \tag{29}$$

which quantifies the relative strength between the flux generated by the helix torque, G, and that due to the force above the wall, $2Fh$. We see that the flow rate is systematically overestimated by the analytical model compared to the simulations though the optimal angle α is almost identical for both models. This overestimation using the RFT is due to the overestimation of the total force $\mathbf{F}$ which becomes more important for larger h.

III. OPTIMAL HELICAL FORM

While the experiments in Ref. 22 exploited the flagella of *E. coli* in order to generate flows, the recent development of artificial bacteria flagella[31,32] suggests that helical shapes

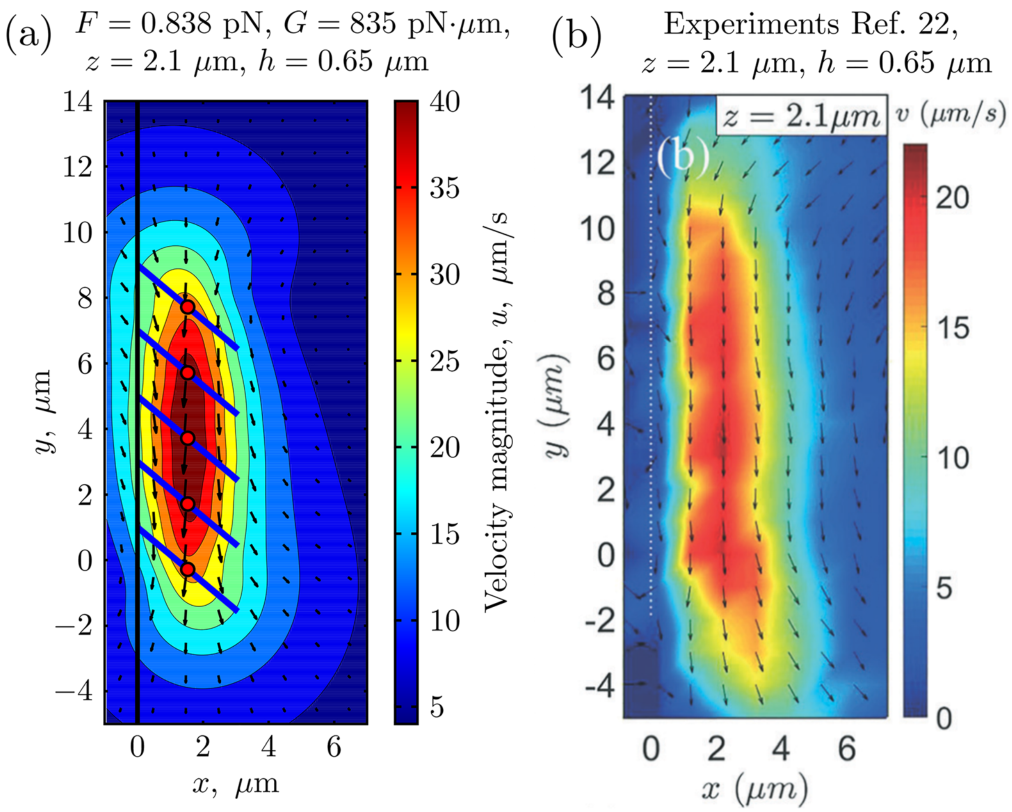

FIG. 6. Velocity vectors and 2D velocity magnitude contours for five helices tilted at angle $\alpha = 40°$, at height $h = 0.65$ μm above the wall. The flow is shown above the helices in the plane $z = 2.1$ μm. The helical axes are denoted by thick blue lines with the red dots in the middle. (a) Flow obtained using the analytical model (RFT) as the superposition of flows due to individual helices; (b) Flow measured experimentally. Reproduced with permission from Gao *et al.*, Lab Chip **15**, 4555–4562 (2015). Copyright 2015 The Royal Society of Chemistry.

different from the biological ones could also be used in order to induce pumping. In this section, we investigate theoretically if a better (artificial) helical filament could be used to drive the flow.

We pose the optimisation problem in the following manner. We wish to maximise the magnitude of the flow rate, Q, given a constrain on the rate of energy dissipation in the fluid, D (which is equal to the rate of working on the rotating helix against the fluid). Using the analytical RFT approximation, the magnitude of the flow rate is given by

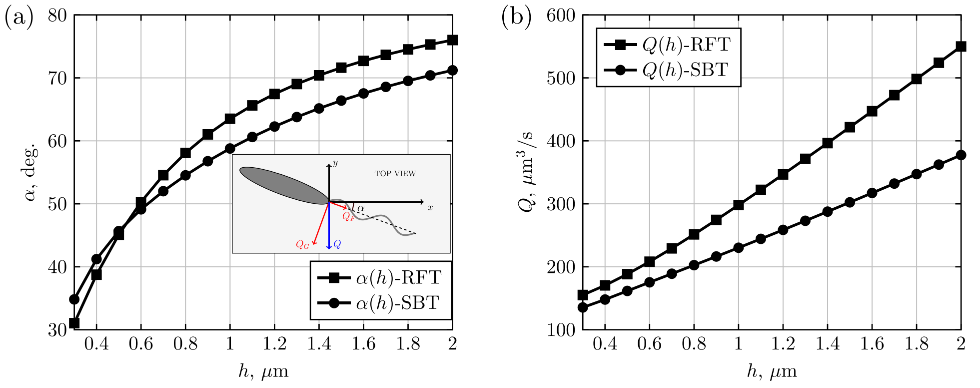

FIG. 7. Comparison between the analytical model (RFT) and the numerical approach (SBT) for (a) the optimal angle α and (b) the flux Q as a function of height h for the helix rotating above the no-slip wall.

$$\begin{aligned}Q^2 &= \left(\frac{Fh}{\pi\mu}\right)^2 + \left(\frac{G}{2\pi\mu}\right)^2,\\ &= \left(\frac{\xi_\perp R\omega(1-\rho)\sin\Psi\cos\Psi Lh}{\pi\mu}\right)^2 + \left(\frac{\xi_\perp R^2\omega(\cos^2\Psi+\rho\sin^2\Psi)L}{2\pi\mu}\right)^2,\end{aligned} \tag{30}$$

while the rate of viscous dissipation in the fluid due to the rotating but not translating helix using Eq. (8) is

$$D = G\omega = \xi_\perp R^2\omega^2(\cos^2\Psi + \rho\sin^2\Psi)L. \tag{31}$$

Let us assume that we wish to keep the dissipation constant, i.e., $D = D_0$, and maximise the magnitude of Q. Substituting L in terms of D_0 into the expression for the flux, one gets the flow rate now given by

$$Q^2 = \left[1 + \left(\frac{2h(1-\rho)\sin\Psi\cos\Psi}{R(\cos^2\Psi+\rho\sin^2\Psi)}\right)^2\right]\left(\frac{D_0}{2\pi\mu\omega}\right)^2. \tag{32}$$

We see that the flux Q is inversely proportional to the angular velocity ω, which means that for a given dissipation, $D_0 = G\omega$, smaller angular velocity ω will lead to a bigger torque G, i.e., a larger flow rate. This can be achieved, for example, by having a longer helix and thus a larger value of L.

For a given total torque on the helix G, what is the shape of the helix which produces the biggest flux Q? In order to find the answer, we need to maximise the force F for the fixed height h. We know that F is linearly proportional to the angular speed ω and the arc length L. Fixing the values of G, ω, h, L, and r sets the dissipation $D_0 = G\omega$, and we aim to determine the helix radius, R, and its pitch, P, so that the flow rate is maximal. This minimisation problem may be formulated using the Lagrangian M and the Lagrange multiplier k given by

$$M(P,R;k) = Q^2(P,R) + k[G(P,R) - G_0], \tag{33}$$

$$Q^2 = \left(\frac{Fh}{\pi\mu}\right)^2 + \left(\frac{G}{2\pi\mu}\right)^2, \tag{34}$$

$$F = \xi_\perp R\omega(1-\rho)\sin\Psi\cos\Psi L, \tag{35}$$

$$G = \xi_\perp R^2\omega(\cos^2\Psi + \rho\sin^2\Psi)L, \tag{36}$$

$$\xi_\parallel = \frac{2\pi\mu}{\ln(0.18P\sec\Psi/r)}, \quad \xi_\perp = \frac{4\pi\mu}{1/2 + \ln(0.18P\sec\Psi/r)}, \tag{37}$$

$$\rho = \frac{\xi_\parallel}{\xi_\perp}, \quad \tan\Psi = \frac{2\pi R}{P}. \tag{38}$$

We numerically solve the resulting Euler-Lagrange equations based on the RFT model

$$\frac{\partial}{\partial P}M(P,R;k) = 0, \quad \frac{\partial}{\partial R}M(P,R;k) = 0, \quad \frac{\partial}{\partial k}M(P,R;k) = 0, \tag{39}$$

in order to determine the extrema for the flux. The solution is shown in Fig. 8(a) as a scatter plot for torques in the range $G_0 = 500, 700, \ldots 3300$ pN μm.

The extrema points (P, R) all lie on the fitted line $R = 0.189P - 0.002\,\mu$m which can be rationalised as follows. Ignoring the weak logarithmic dependence of $\xi_\parallel, \xi_\perp$ on R, P we can in

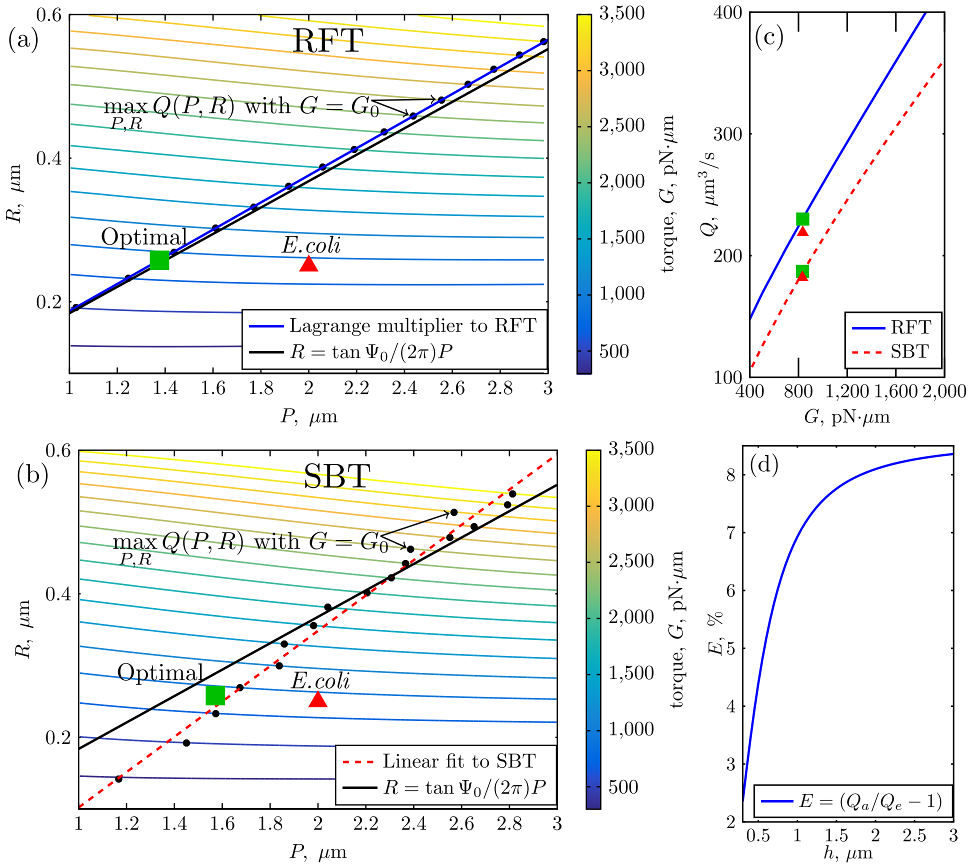

FIG. 8. (a) and (b) Contours values of the torque, G, as a function of the helix radius, R, and pitch, P. Torques computed using the analytical model (RFT, a) and the numerical model (SBT, b). The scatter plots show the discrete values of R, P that maximise Q given the torque values $G_0 = 500, 700, \ldots 3300$ pN μm. (c) Optimal flux, Q, as a function of the applied torque, G. (d) Marginal increase in the flux, E, using the optimal helix versus the *E. coli* helix as a function of distance to the wall, h. In (a)–(c) the red triangles denote the values of pitch, radius, torque, and flux for the *E. coli* bacterium, while the green square shows the optimal radius, pitch, and flux for the same torque as *E. coli*.

fact find analytically the optimal values of R, and P which maximise the flux for a given torque namely

$$\frac{2\pi R}{P} = \tan\Psi_0 = \rho^{-1/4}. \tag{40}$$

This analytical solution is shown as a black line in Fig. 8(a) and is very close to the blue line (numerical calculations). In this figure, we also use the red triangle to denote the radius and pitch for the flagellar filament of *E. coli*, while the green square denotes the optimal radius and the pitch for pumping such that the torque is the same as that generated the *E. coli* bacterium. In the case of *E. coli*, it was reported that the torque applied by the rotary motor remains approximately constant up to a relatively high rotation frequency (170 Hz at 23 °C),[33,34] and we use this biological value of 830 pN μm for G.

We may then calculate the radius, pitch, flux, and the optimal angle in terms of the fixed quantities for the optimal shape, i.e., when $\tan\Psi = \rho^{-1/4}$ and obtain

$$R = \left(\frac{G_0}{\xi_\perp \omega L}\right)^{1/2} \cdot \rho^{-1/4}, \tag{41}$$

$$P = 2\pi\rho^{1/4}R = 2\pi\left(\frac{G_0}{\xi_\perp \omega L}\right)^{1/2}, \tag{42}$$

$$Q^2 = \left(\frac{\xi_\perp RL\omega(\rho^{1/4} - \rho^{3/4})h}{\pi\mu}\right)^2 + \left(\frac{G_0}{2\pi\mu}\right)^2, \tag{43}$$

$$Q^2 = \left(\frac{\xi_\perp^{1/2} L^{1/2}\omega^{1/2} G_0^{1/2}(1 - \rho^{1/2})h}{\pi\mu}\right)^2 + \left(\frac{G_0}{2\pi\mu}\right)^2, \tag{44}$$

$$\tan\alpha = 2\xi_\perp^{1/2} L^{1/2}\omega^{1/2} G_0^{-1/2} h(1 - \rho^{1/2}). \tag{45}$$

Surprisingly, the optimal pitch P is independent of the drag ratio ρ but is only a function of the applied torque G_0, the helix length L, the rotation frequency ω, and the drag coefficient $\xi_\perp$.

Instead of the analytical modelling approach, we may instead compute the flux Q as a function of the parameters of the helix, R, P, using the numerical model (SBT) with a fixed helix height above the wall $h = 0.65\,\mu$m. These results are shown in Fig. 8(b). The contours of the torque G as the function of the helix radius R and the pitch P match well the ones calculated using the analytical model (RFT). In both cases, the contours are almost horizontal when the radius R is small, e.g., about $0.25\,\mu$m in the case of *E. coli*. This can be justified by examining the form of torque

$$G = \xi_\perp R^2\omega(\cos^2\Psi + \rho\sin^2\Psi)L = \xi_\perp R^2\omega L\left(\frac{P^2 + 4\pi^2\rho R^2}{P^2 + 4\pi^2 R^2}\right). \tag{46}$$

The torque depends weakly on the pitch P, especially when the helix radius R is small. This means that the contours of G are approximately $G(R, P) \sim R^2 = \text{const}$, i.e., horizontal contour lines.

The optimal value of the flux, Q, is plotted in Fig. 8(c) as a function of the applied torque, G. We see that the analytical model systematically overestimates the flux compared with the computational approach. Remarkably, the difference between the flow rate produced by the *E. coli* bacterium and the optimal one for the same applied torque is only 3%, revealing that the bacterial flagellar filaments are almost at the optimal shape to pump the fluid over the surface. How does this result depend on the distance to the surface? We may compute the ratio between the flux Q_a due to the optimal artificial helix (force F_a, torque G_0) versus the flux Q_e due to the *E. coli* shaped helix (force F_e, torque G_0)

$$E = \frac{Q_a}{Q_e} - 1 = \left(\frac{G_0^2/(2\pi\mu)^2 + F_a^2 h^2/(\pi\mu)^2}{G_0^2/(2\pi\mu)^2 + F_e^2 h^2/(\pi\mu)^2}\right)^{1/2} - 1, \tag{47}$$

$$E = \left(1 + \frac{F_a^2 h^2 - F_e^2 h^2}{G_0^2/4 + F_e^2 h^2}\right)^{1/2} - 1 = \left(1 + \frac{(F_a/F_e)^2 - 1}{1 + G_0^2/(4F_e^2 h^2)}\right)^{1/2} - 1. \tag{48}$$

The applied torque calculated analytically is $G_0 = 835$ pN$\,\mu$m. The biological force is $F_e = 0.838$ pN, while the optimal force is $F_a = 0.910$ pN. We see in Fig. 8(d) that the percentage increase in flow rate between the biological value and the optimal value is always in the range 3%–8% and increases with the height above the wall. Bacterial filaments thus seem to be nearly optimal for pumping fluid very close to a surface, a result which could be important in the context of efficient expansion of bacterial swarms.[35]

IV. CONCLUSION

Our simple analytical (RFT) and computational (SBT) models are able to capture the leading-order physics of the fluid flux produced by a rotating helical bundle of flagellar filaments near a no-slip wall. Fluid is being pumped along the flagellar axis because of the net force acting on the fluid and in the direction perpendicular to the flagellar axis because of the rotation in the presence of the wall. The force produces a flow rate $Q_F = Fh/(\pi\mu)$ which depends on the distance to the wall h, whereas the torque produces the flux $Q_G = G/(2\pi\mu)$. The combined effect of force and torque implies that the net flow rate is directed at an angle to the flagellum, whose value depends on the helix parameters and its distance to the wall. While our model is limited to the cases where the boundary affecting the fluid flow is a flat no-slip wall, more advanced numerical techniques would be needed to tackle complex boundaries such as channels, corners, and irregular surfaces. Importantly, our theoretical predictions agree with the numerical and experimental results in Ref. 22, and thus provide fundamental understanding of the relationship between orientation and flow pumping, setting the stage for the future development of efficient micropumps not only using bacteria but also other actuation methods (e.g., magnetic).

We next investigate the optimal shape of the helix in terms of its radius R and pitch P assuming a fixed applied torque G, total helical length L, angular speed ω, height above the wall h, and filament radius r. We find that nearly optimal pumping is achieved when the helix pitch angle is fixed and equal to $\tan\Psi = 2\pi R/P = \rho^{-1/4}$, where ρ is the ratio between the drag coefficients. With a drag ratio $\rho = 1/2$, one finds that Ψ is close to 50°. While the pitch angle for normal flagellar filaments is close to 40° and is optimised for propulsion,[36] the theoretically optimal pumping helix performs only 3% to 8% better than *E. coli* depending on the height above the wall. This is a very small difference indicating that bacterial flagella are very efficient micropumps, a result which could be relevant to the expansion of bacterial swarms[37] or the future development of biological micropumps to be used for automation in chemistry and biology.[19]

ACKNOWLEDGMENTS

This work was funded in part by an ERC Consolidator grant from the European Union (EL).

APPENDIX A: POINT FORCE ABOVE AN INFINITE WALL AT $Z = 0$

Consider a Stokeslet placed at $\mathbf{y}_0 = (0,0,h)$. Define $\mathbf{r} = \mathbf{x} - \mathbf{y_0} = (x, y, z-h)$ and $\mathbf{R} = (x, y, z+h)$. The solution for a Stokeslet in the vicinity of a stationary plane boundary is[26,27]

$$u_i = \frac{F_j}{8\pi\mu}\left[\left(\frac{\delta_{ij}}{r} + \frac{r_i r_j}{r^3}\right) - \left(\frac{\delta_{ij}}{R} + \frac{R_i R_j}{R^3}\right)\right] + \frac{F_j}{8\pi\mu}\left[2h(\delta_{j\alpha}\delta_{\alpha k} - \delta_{j3}\delta_{3k})\frac{\partial}{\partial R_k}\left\{\frac{hR_i}{R^3} - \left(\frac{\delta_{i3}}{R} + \frac{R_i R_3}{R^3}\right)\right\}\right]. \tag{A1}$$

We are interested in the Stokeslet parallel to the wall; therefore, without loss of generality we choose $\mathbf{F} = (F_1, 0, 0)$. Let us calculate the flux in the plane perpendicular to the Stokeslet

$$Q_1 = \int_0^\infty \int_{-\infty}^\infty u_1 dy\, dz. \tag{A2}$$

Expand the flow to the leading order in h and integrate to get

$$u_1 = \frac{F_1}{8\pi\mu}\left[\frac{12x^2 zh}{(x^2+y^2+z^2)^{5/2}} + \mathcal{O}(h^2)\right], \quad Q_1 = \frac{F_1 h}{\pi\mu}\cdot . \tag{A3}$$

Therefore, there is a finite flow rate produced in the direction of the Stokeslet given by

$$\mathbf{Q} = \frac{\mathbf{F}_{\parallel} h}{\pi \mu}, \tag{A4}$$

where $\mathbf{F}_{\parallel} = (F_1, F_2, 0)$. Note that the flux is zero if the force is perpendicular to the wall, as expected by symmetry.

APPENDIX B: POINT TORQUE ABOVE AN INFINITE WALL AT $Z = 0$

Consider now a Rotlet placed at $\mathbf{y_0} = (0, 0, h)$. Define $\mathbf{r} = \mathbf{x} - \mathbf{y_0} = (x, y, z - h)$ and $\mathbf{R} = (x, y, z + h)$. The solution for the Rotlet in the vicinity of a stationary plane boundary is[26,27]

$$u_i = \frac{G_j \epsilon_{ijk}}{8\pi\mu}\left[\frac{r_k}{r^3} - \frac{R_k}{R^3}\right] + \frac{G_j \epsilon_{kj3}}{8\pi\mu}\left[2h\left(\frac{\delta_{ik}}{R^3} - \frac{3R_i R_k}{R^5}\right) + \frac{6R_i R_k R_3}{R^5}\right]. \tag{B1}$$

Since we are interested in the Rotlet parallel to the wall, we choose $\mathbf{G} = (0, G_2, 0)$. The flux produced by this Rotlet when it is above the no-slip wall is

$$Q_1 = \int_0^{\infty}\int_{-\infty}^{\infty} u_1 dy\, dz, \quad Q_2 = 0, \quad Q_3 = 0. \tag{B2}$$

Expanding the flow to the order in h and integrate we obtain

$$u_1 = \frac{G_2}{8\pi\mu}\left[\frac{6x^2 z}{(x^2 + y^2 + z^2)^{5/2}} + \mathcal{O}(h)\right], \quad Q_1 = \frac{G_2}{2\pi\mu} \cdot . \tag{B3}$$

So in general the flux is given by

$$\mathbf{Q} = \frac{\mathbf{G}_{\parallel} \times \mathbf{e}_z}{2\pi\mu}, \tag{B4}$$

where $\mathbf{G}_{\parallel} = (G_1, G_2, 0)$ and here again the flux is zero if the torque is perpendicular to the wall.

[1] C. Kunert, J. W. Baish, S. Liao, T. P. Padera, and L. L. Munn, "Mechanobiological oscillators control lymph flow," Proc. Natl. Acad. Sci. U. S. A **112**, 10938–10943 (2015).

[2] I. M. Glynn, "Annual review prize lecture. All hands to the sodium pump," J. Physiol. **462**, 1–30 (1993).

[3] K. H. Jensen, J. Liesche, T. Bohr, and A. Schulz, "Universality of phloem transport in seed plants," Plant Cell Environ. **35**, 1065–1076 (2012).

[4] R. Faubel, C. Westendorf, E. Bodenschatz, and G. Eichele, "Cilia-based flow network in the brain ventricles," Science **353**, 176–178 (2016).

[5] J. V. Fahy and B. F. Dickey, "Airway mucus function and dysfunction," N. Engl. J. Med. **363**, 2233–2247 (2010).

[6] N. Spassky and A. Meunier, "The development and functions of multiciliated epithelia," Nat. Rev. Mol. Cell Biol. **18**, 423–436 (2017), https://www.ncbi.nlm.nih.gov/pubmed/28400610.

[7] A. Nisar, N. Afzulpurkar, B. Mahaisavariya, and A. Tuantranont, "MEMS-based micropumps in drug delivery and biomedical applications," Sens. Actuators, B **130**, 917–942 (2008).

[8] F. Abhari, H. Jaafar, and N. A. Md. Yunus, "A comprehensive study of micropumps technologies," Int. J. Electrochem. Sci. **7**, 9765–9780 (2012).

[9] C. Zhou, H. Zhang, Z. Li, and W. Wang, "Chemistry pumps: A review of chemically powered micropumps," Lab Chip **16**, 1797–1811 (2016).

[10] A. Sokolov, M. M. Apodaca, B. A. Grzybowski, and I. S. Aranson, "Swimming bacteria power microscopic gears," Proc. Natl. Acad. Sci. **107**, 969–974 (2010).

[11] R. Di Leonardo, A. Búzás, L. Kelemen, G. Vizsnyiczai, L. Oroszi, and P. Ormos, "Hydrodynamic synchronization of light driven microrotors," Phys. Rev. Lett. **109**, 034104 (2012).

[12] M. J. Kim and K. S. Breuer, "Microfluidic pump powered by self-organizing bacteria," Small **4**, 111–118 (2008).

[13] E. B. Steager, M. S. Sakar, D. H. Kim, V. Kumar, G. J. Pappas, and M. J. Kim, "Electrokinetic and optical control of bacterial microrobots," J. Micromech. Microeng. **21**, 035001 (2011).

[14] R. W. Carlsen and M. Sitti, "Bio-hybrid cell-based actuators for microsystems," Small **10**, 3831–3851 (2014).

[15] N. Uchida and R. Golestanian, "Synchronization and collective dynamics in a carpet of microfluidic rotors," Phys. Rev. Lett. **104**, 178103 (2010).

[16] J. D. Martindale and H. C. Fu, "Autonomously responsive pumping by a bacterial flagellar forest: A mean-field approach," Phys. Rev. E **96**, 033107 (2017).

[17] N. Darnton, L. Turner, K. Breuer, and H. C. Berg, "Moving fluid with bacterial carpets," Biophys. J. **86**, 1863–1870 (2004).

[18] M. J. Kim and K. S. Breuer, "Use of bacterial carpets to enhance mixing in microfluidic systems," J. Fluids Eng. **129**, 319–324 (2007).

[19] T. M. Squires and S. R. Quake, "Microfluidics: Fluid physics at the nanoliter scale," Rev. Mod. Phys. **77**, 977–1026 (2005).

[20] S. Tung, J. Kim, A. Malshe, C. C. Lee, and R. Pooran, "A cellular motor driven microfluidic system," in *12th International Conference on TRANSDUCERS, Solid-State Sensors, Actuators and Microsystems* (IEEE, 2003), Vol.1, pp. 678–681.

[21] S. Tung and J. Kim, "Microscale hybrid devices powered by biological flagellar motors," IEEE Trans. Autom. Sci. Eng. **3**, 260–263 (2006).

[22] Z. Gao, H. Li, X. Chen, and H. P. Zhang, "Using confined bacteria as building blocks to generate fluid flow," Lab Chip **15**, 4555–4562 (2015).

[23] J. Lighthill, "Flagellar hydrodynamics," SIAM Rev. Soc. Ind. Appl. Math. **18**, 161–230 (1976).

[24] R. E. Johnson, "An improved slender-body theory for Stokes flow," J. Fluid. Mech. **99**, 411–431 (1980).

[25] A. Tornberg and M. J. Shelley, "Simulating the dynamics and interactions of flexible fibers in stokes flows," J. Comput. Phys **196**, 8–40 (2004).

[26] J. R. Blake, "Singularities of viscous flow," J. Eng. Math. **8**, 113–124 (1974).

[27] J. R. Blake and A. T. Chwang, "Fundamental singularities of viscous flow," J. Eng. Math. **8**, 23–29 (1974).

[28] H. C. Berg, *E. coli in Motion* (Springer Science & Business Media, 2008).

[29] L. Turner, W. S. Ryu, and H. C. Berg, "Real-time imaging of fluorescent flagellar filaments," J. Bacteriol. **182**, 2793–2801 (2000).

[30] E. Lauga and T. R. Powers, "The hydrodynamics of swimming microorganisms," Rep. Prog. Phys. **72**, 096601 (2009).

[31] L. Zhang, K. E. Peyer, and B. J. Nelson, "Artificial bacterial flagella for micromanipulation," Lab Chip **10**, 2203–2215 (2010).

[32] S. Tottori, L. Zhang, F. Qiu, K. K. Krawczyk, A. Franco-Obregón, and B. J. Nelson, "Magnetic helical micromachines: Fabrication, controlled swimming, and cargo transport," Adv. Mater. **24**, 811–816 (2012).

[33] X. Chen and H. C. Berg, "Torque-speed relationship of the flagellar rotary motor of Escherichia coli," Biophys. J. **78**, 1036–1041 (2000).

[34] A. L. Nord, Y. Sowa, B. C. Steel, C. Lo, and R. M. Berry, "Speed of the bacterial flagellar motor near zero load depends on the number of stator units," PNAS **114**, 11603–11608 (2017).

[35] Y. Wu, B. G. Hosu, and H. C. Berg, "Microbubbles reveal chiral fluid flows in bacterial swarms," Proc. Natl. Acad. Sci. U. S. A. **108**, 4147–4151 (2011).

[36] S. E. Spagnolie and E. Lauga, "Comparative hydrodynamics of bacterial polymorphism," Phys. Rev. Lett. **106**, 058103 (2011).

[37] D. B. Kearns, "A field guide to bacterial swarming motility," Nat. Rev. Microbiol. **8**, 634–644 (2010).